Chemical Engineering Journal 378 (2019) 122212

Contents lists available at ScienceDirect

Chemical Engineering Journal

journal homepage: www.elsevier.com/locate/cej

Enhanced cycling performance of Si-MXene nanohybrids as anode for high performance lithium ion batteries

Xiaoquan Zhu, Jiale Shen, Xifan Chen, Yang Li, Wenchao Peng, Guoliang Zhang, Fengbao Zhang, Xiaobin Fan*

School of Chemical Engineering and Technology, State Key Laboratory of Chemical Engineering, Collaborative Innovation Center of Chemical Science and Engineering, Tianjin University, Tianjin 300072, People's Republic of China

HIGHLIGHTS

- The sandwiched structure of Si/Ti_3C_2 hybrid release the strain of Si particles.
- The Ti_3C_2 layers can effectively alleviate volume variation of Si anode.
- The Si/Ti_3C_2 hybrid shows improved cycling performance than pristine Si.

ARTICLE INFO

Keywords:
Si anode
MXene
Sandwich-structure
Lithium ion batteries

ABSTRACT

The practical application of Si anodes is hampered by huge volume expansion during lithiation/delithiation process, leading to poor cycling performance and electrode fracture. To overcome such weakness, a sandwich-like Si/d-Ti_3C_2 hybrids are fabricated and show an excellent reversible capacity of 1130 mA h g^{-1} at a current density of 500 mA g^{-1} after 200 cycles. Comparing with pristine Si, the improved electrochemical performance of Si/d-Ti_3C_2 hybrids can be attributed to the fact that the d-Ti_3C_2 MXene can significantly enhance the electronic conductivity of electrode and support integrity of electrodes. The Si/d-Ti_3C_2 hybrids perform their promising prospect in lithium ion batteries.

1. Introduction

Lithium-ion batteries (LIBs) are the most popular types of rechargeable batteries for portable devices, electric vehicles and so on. However, the limited theoretical specific capacity (372 mA h g^{-1}) of traditional graphite anode materials can't meet the increasing demands in high energy density batteries [1]. Thus a large number of materials with high-specific-capacity could be applied in anodes have attracted tremendous interests. Silicon (Si) with high theoretical capacity (4200 mA h g^{-1}, lithiated to $Li_{4.4}Si$) and low working potential (0.5 V vs. Li/Li^+) become one of the most promising anode candidates among them [2–4]. Nevertheless, the practical application of Si anode is still hindered by some major problems, especially the huge volumetric fluctuations (~300%) during lithiation/delithiation processes and its low intrinsic electrical conductivity ($< 10^{-3}$ S cm^{-1} at 25 °C) [5]. The large volume change would induce pulverization, and reduce the contact or even cause the detachment of the active material from the current collectors [6]. Besides, the repeated volume expansion and shrinkage result in the regeneration of the solid electrolyte interphase (SEI) and collapse of electrode structure.

Therefore, many strategies have been developed to improve the electrochemical cyclability of Si anodes. For example, the binder designs and electrolytes are explored to stabilize the electrochemical performance of Si anodes [7,8]. Variation of nanostructures has been also made to improve the stability of Si anode by alleviating the strain and huge volume change, including the alternation of nano-structured Si materials and hybrids combination [9–15]. It is found that Si particles with reduced size show the reduced tendency for the particle cracking [16–18]. Many stress-relief buffer matrixes have also been introduced to accommodate the volume change of Si during repeat cycles [19,20]. The stress from the volume variation of Si can be released quickly by the matrix. Generally, carbonaceous matrices have been regarded as the ideal candidate to hybrid with Si, owing to their high electric conductivity and low cost [21–23]. For example, Guo group synthesized the watermelon like Si/C microsphere showing a high reversible capacity of 620 mA h g^{-1} at a high area capacity of

* Corresponding author.
E-mail address: xiaobinfan@tju.edu.cn (X. Fan).

https://doi.org/10.1016/j.cej.2019.122212
Received 30 March 2019; Received in revised form 20 June 2019; Accepted 10 July 2019
Available online 11 July 2019
1385-8947/

2.54 mA h cm^{-2} [24]. Another group reported that the graphene not only relieve the stress from the Fe_2O_3 nanoparticles during Li uptake/release, but also facilitate electron transport [25]. To tackle the problem of the regeneration of solid electrolyte interphase (SEI). Cui et al. designed yolk-shell structure with Si nanoparticles to address the problems of volume expansion and unstable SEI interface, the Coulombic efficiency is significantly improved [26,27].

The exfoliated transition metal carbide and nitride (MXene), which have graphene-like two-dimensional (2D) structure, show promising applications in energy storage [28–30]. The $Ti_3C_2T_x$ (T represents the terminal functional groups, such as –O, –OH, –F) have attracted particular attention, owing to its excellent metallic conductivity and high volumetric capacity [31–33]. The large-scale production of $Ti_3C_2T_x$ MXene is still restricted by the using of toxic chemical in the etching step. Recently, many methods by using less toxic chemical have been proposed. The $Ti_3C_2T_x$ layers could be obtained by HF etching and TMAOH delamination [34]. It has been demonstrated that the Al atom layers in the MAX phase could be etched by LiF + HCl route [35]. These progresses in the preparation of MXene will facilitate the application of MXene in the future. The electrical conductivity of $Ti_3C_2T_x$ MXene is much better than graphene [36]. The abundant surface functional groups of the $Ti_3C_2T_x$ could provide ideal sites for surface anchoring. Thus the $Ti_3C_2T_x$ MXene has been used in supercapacitors, LIBs and other energy storage units [37–41]. However, there are few researches focus on the electrochemical performance of Si/MXene hybrid as LIBs anode. In this study, the series sandwich-like Si/$Ti_3C_2T_x$ hybrids with different mass ratios are fabricated through a facile and scalable method, and their electrochemical performance have been systematically investigated (Fig. 1a). The Si/d-Ti_3C_2 (2:1) hybrids show excellent reversible capacity of 1130 mA h g^{-1} at a current density of 500 mA g^{-1} after 200 cycles.

2. Experimental section

2.1. Materials synthesis

The obtained Ti_3AlC_2 were treated by immersing in HF solution (40%) for 18 h with a concentration of 0.1 g mL^{-1}. Then the suspension was washed with deionized water until the pH of the liquid reached 5–6. The wet sediment was dispersed in 25% aqueous tetramethylammonium hydroxide (TMAOH) for 12 h with shaking. The TMA^+ intercalated Ti_3C_2 MXene was obtained by centrifuge, then redispersed in 300 mL H_2O. To remove the excess residual TMA^+ and OH^-, resulting suspension was washed with deionized water three times. After that, the dispersion was centrifuged at low speed (2000 rpm) to remove un-exfoliated Ti_3C_2 nanosheets and form the stable solution. Finally, a stable ink of Ti_3C_2 nanosheets, with a concentration of ~1.0 mg mL^{-1} was obtained.

The hybrids with different mass ratio of Si particles to d-Ti_3C_2 were synthesized to optimize their cycling performance. The 100 mg Si nanoparticles (~100 nm) were dispersed in 50 mL mixture of alcohol and water (v/v = 1:1). The solution was sonicated for 20 min to obtain Si suspension. Then 50 mL Ti_3C_2 ink was mixed with silicon aqueous solution. The mixed solution was sonicated for 30 min, and then filtered through a polyvinylidene fluoride filter (0.22 μm pore size). The product was dispersed in 10 mL water, and then frozen and freeze-dried for a few days. At last, the obtained samples were dried in vacuum dryer for 10 h in 80 °C. In the full text, the Si/d-Ti_3C_2 is used to represent the Si/d-Ti_3C_2 (2:1) hybrids with mass ratio of 2:1.

2.2. Materials characterization

Powder X-ray diffraction (XRD) measurements were obtained using

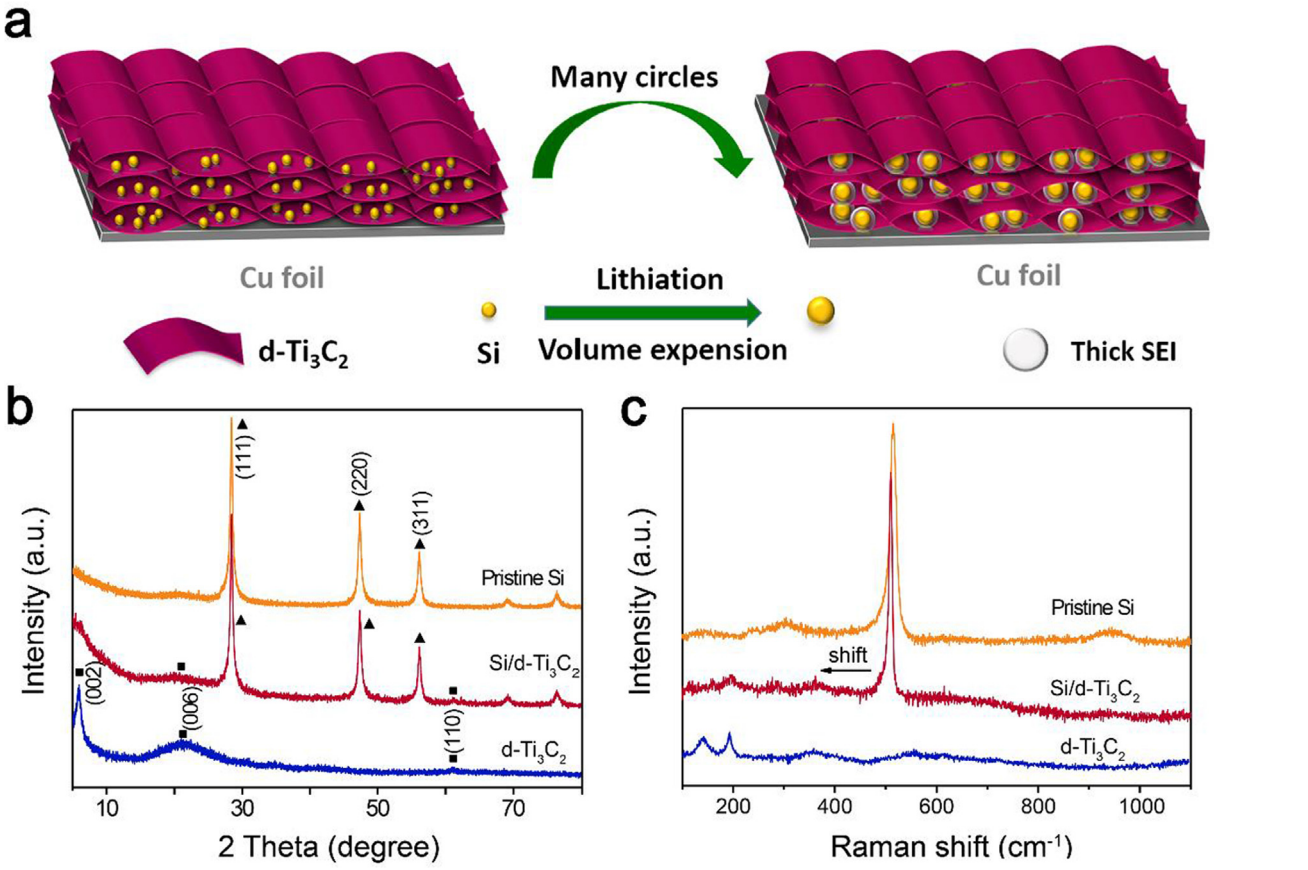

Fig. 1. (a) Illustration of the sandwich-like Si/d-Ti_3C_2 hybrids as electrode of LIBs. (b) XRD patterns of pristine Si nanoparticles, d-Ti_3C_2 and Si/Ti_3C_2 hybrids, respectively. (c) The Raman spectra of the pristine Si nanoparticles, d-Ti_3C_2 and Si/d-Ti_3C_2 hybrids, respectively.

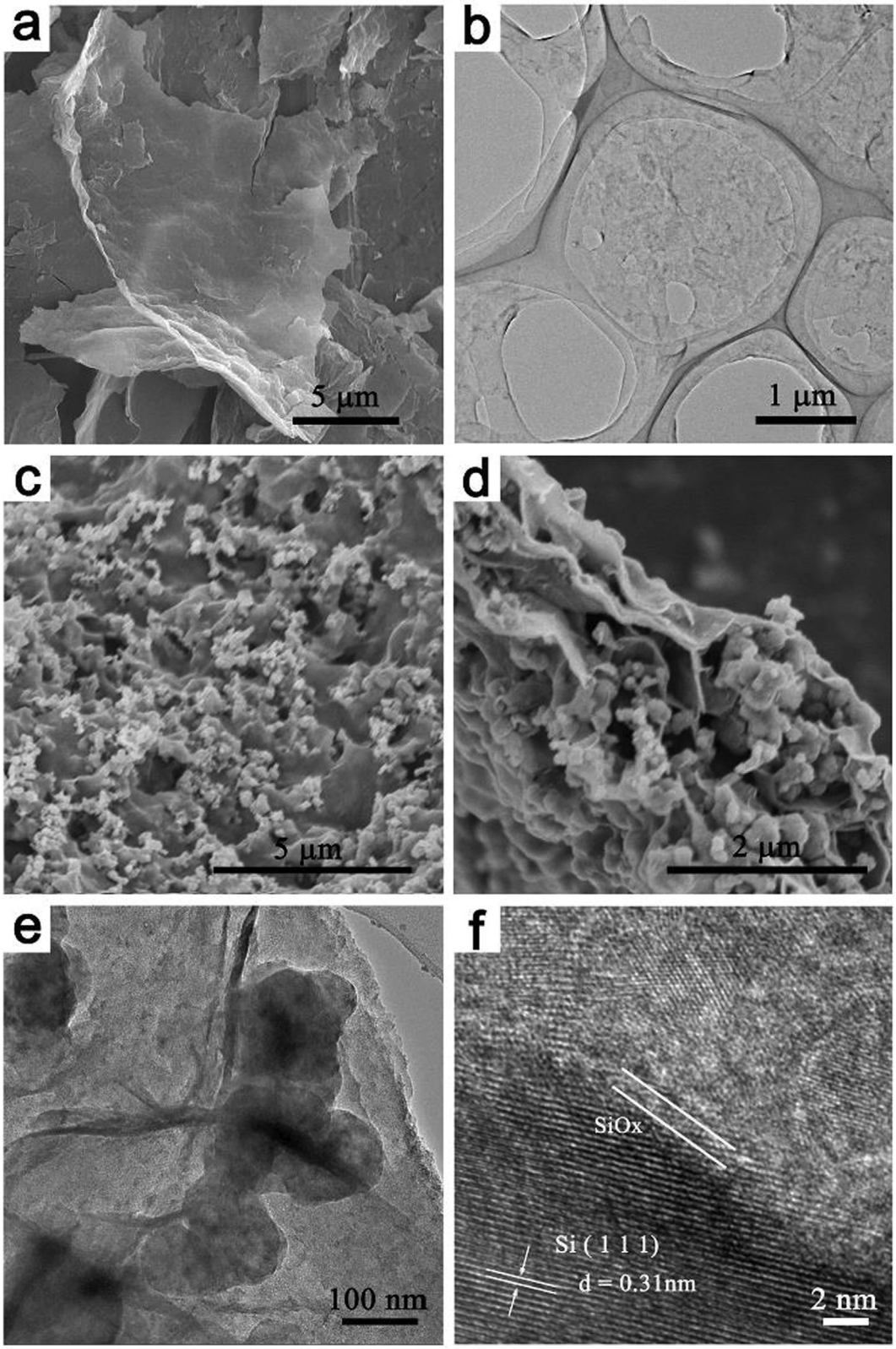

Fig. 2. (a) The SEM and (b) TEM images of d-Ti_3C_2 layers (c) SEM and (d) cross-sectional SEM images of Si/d-Ti_3C_2 hybrids. (e) TEM and (f) high-resolution TEM images of Si/d-Ti_3C_2 hybrids.

an X-ray diffractometer (D8-Focus, Bruker Axs with Cu-Kα radiation, λ = 1.54178 Å). The morphology and microstructure were characterized with a scanning electron microscope (SEM, S-4800, HITACHI) a transmission electron microscope (TEM, JEM-2100F, JEOL). X-ray photoelectron spectroscopy (XPS) was carried out on the (ESCALAB-210XI, Thermo Scientific) with $Al_{K\alpha}$ radiation. Raman spectra were measured on a Raman spectrometer (LabRam HR Evolution, HORIBA) using a laser of 532 nm at room temperature. Fourier transform infrared

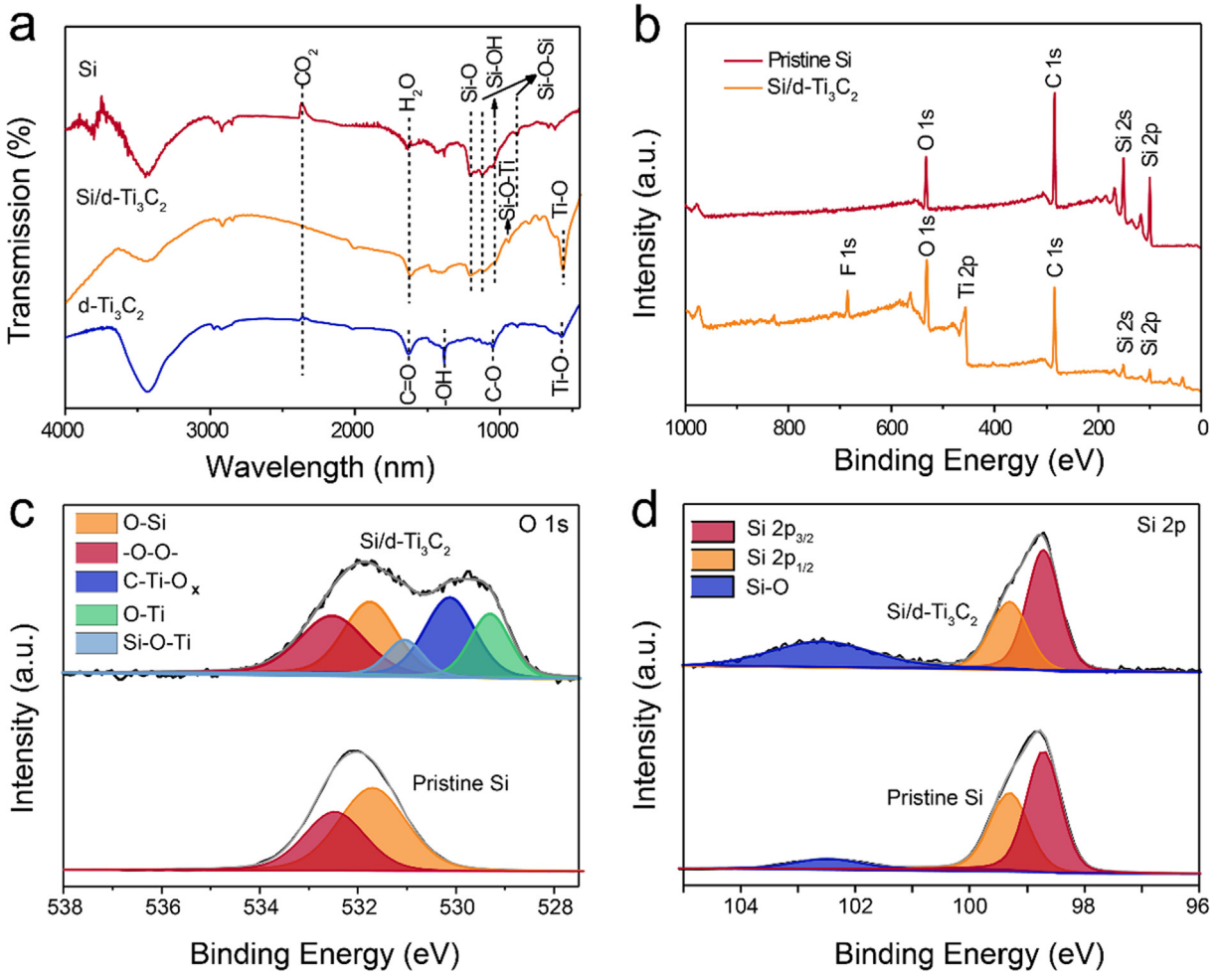

Fig. 3. (a) The FT-IR of the pristine Si, Si/d-Ti_3C_2 hybrids and d-Ti_3C_2, respectively; (b) XPS survey spectra of pristine Si and Si/d-Ti_3C_2 hybrids, and corresponding high-resolution of (c) O 1s and (d) Si 2p spectrum.

(FTIR) of the samples were recorded on a Thermo Nicolet Nexus spectrometer in the 4000–400 cm^{-1} range using powdered samples diluted in KBr pellets. Atomic force microscopy (AFM) image was obtained from (AFM, CSPM5500, BENYUAN).

2.3. Electrochemical measurements

The working electrodes were prepared through coating the copper foil with a homogeneous slurry consisting of active materials (Si-based material), Super P, sodium alginate with a mass ratio of 65:20:15, then the electrode was dried under vacuum at 100 °C for 10 h. On average, the electrode mass loading was about 1.3 mg cm^{-2}. CR2032-type coin cells were assembled in an Ar-filled glove box to evaluate the electrochemical properties of Si-based anodes. The coin cell was composed of a pure lithium foil as the counter electrode, Celgard 2400 as the separator, and 1 M $LiPF_6$ in a mixture of ethylene carbonate and dimethyl carbonate (v/v = 1:1) containing 5% fluoroethylene carbonate as the electrolyte. The galvanostatically charged and discharged in the voltage range of 0.01–1.0 V vs. Li/Li^+ using a Land Battery Tester (Land CT 2001 A, Wuhan, China). Cyclic voltammetry (CV) was carried out on an electrochemical workstation (CHI 760, China) at a scan rate of 0.01 mV s^{-1} in the voltage range of 0.01–1.0 V vs. Li/Li^+. The electrochemical impedance spectroscopy (EIS) measurements were performed on an electrochemical workstation (CHI 760, China) in the frequency range of 100 kHz to 10 mHz with an AC perturbation of 5 mV. We disassembled the batteries in the glove box. Then the electrodes were rinsed with ethylene carbonate and dimethyl carbonate to remove the residual lithium salt. After dried for several hours in the glove box, the electrodes were adhered to XRD sample stages. Then we put these stages into the ziplock bag to avoid oxidation. The samples were taken out and measured as soon as possible when conducting the XRD measurement.

3. Results and discussion

In brief, the $Ti_3C_2T_x$ MXene layers were obtained by HF etching and TMAOH delamination. The XRD and SEM information of pristine Ti_3AlC_2 and HF-etched $Ti_3C_2T_x$ were shown in Fig. S1. The (0 0 2) peak of HF-etched $Ti_3C_2T_x$ shifts to the lower angle, indicating the increased interlayer spacing. The disappearance of peak at $2\theta = 39°$ demonstrates that the Al atom layers have been completely etched. After TMAOH delamination, the d-Ti_3C_2 layers exhibit the characteristic (0 0 2), (0 0 6) and (1 1 0) diffractions (Fig. 1b). The main (0 0 2) peak shifts to $2\theta = 6.02°$ corresponding to an interlayer spacing of ~14.6 Å [34]. Compared with the pristine Ti_3AlC_2, the HF-etched $Ti_3C_2T_x$ has a loosely packed accordion-like structure. However, the (0 0 2) peak of Si/d-Ti_3C_2 hybrids almost disappears. This is attributed to the Si nanoparticles sandwiched between the adjacent d-Ti_3C_2 nanosheets could prevent from restacking of d-Ti_3C_2 MXene [42].

In order to further investigate the conformation about the Si/d-Ti_3C_2 hybrids, the obtained samples are characterized by Raman spectra (Fig. 1c). The enlarged curve of d-Ti_3C_2 is shown in Fig. S2. The peaks at 197.5 and 721 cm^{-1} are typically attributed to symmetry out-of-plane vibrations of Ti and C atoms, respectively. The modes at 366

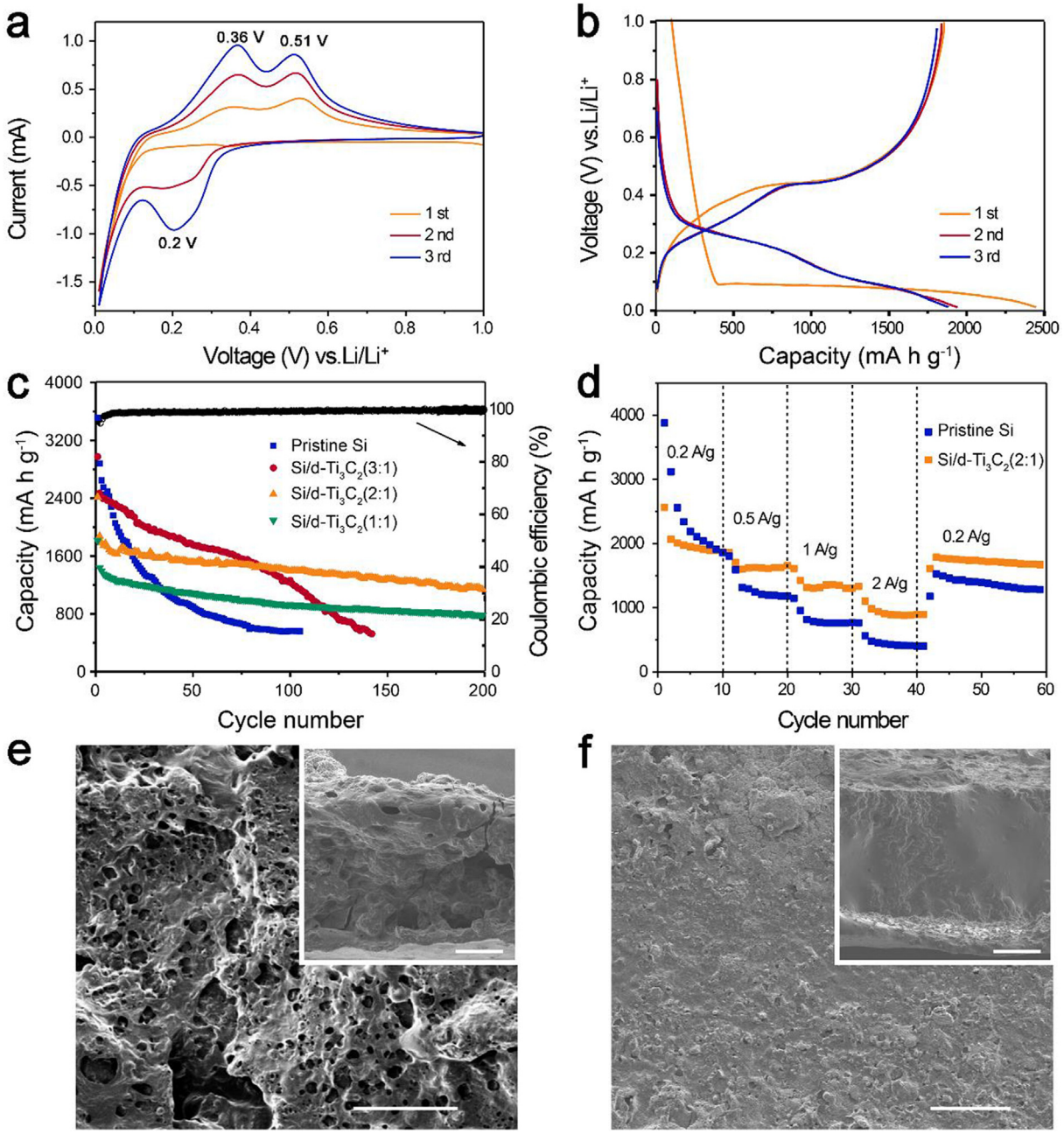

Fig. 4. (a) Cyclic voltammetry profiles of the Si/d-Ti_3C_2 (2:1) hybrids for the first three cycles. (b) Galvanostatic discharge–charge curves of Si/d-Ti_3C_2 (2:1) hybrids for the first three cycles. (c) Cycling performance of the Si/d-Ti_3C_2 hybrids with different mass ratios at a current density of 500 mA g^{-1}. (d) Rate capability of Si/d-Ti_3C_2 (2:1) hybrids and pristine Si nanoparticles. (e) SEM images of pristine Si anodes and (f) Si/Ti_3C_2 anode after 50 cycles. The scale bar is 150 μm. The insert images are the cross-sectional SEM images of corresponding electrodes. The scale bar is 20 μm.

and 624 cm^{-1} correspond to Eg group vibrations. The vibration signal of TiO_2 (144.5 cm^{-1}) suggests that the surface of d-Ti_3C_2 nanosheets might be oxidized slightly [43,44]. The pristine Si exhibits a strong Raman peak at 507 cm^{-1}, which is ascribed to the scattering of first order optical phonon and the response of Si–Si stretching vibration. Other two broad peaks at 297 and 934 cm^{-1} are assigned to the overtones of phonon modes of second-order Raman spectrum of Si. In the Raman spectrum of Si/d-Ti_3C_2 hybrids, the presence of peaks at 197 and 366 cm^{-1} is associated with the vibrations of d-Ti_3C_2 layer. The high-intensity Si signals press the peaks of d-Ti_3C_2 seriously. In addition, the vibration peaks of Si NPs exhibit a small shift to higher wavenumbers, comparing with that of pristine Si. Such shift may be resulted from the reduced interparticle strain in the hybrids [45]. It facilitates the stress relief of the as-synthesized electrode during volume variation.

The morphology of the samples is characterized by SEM and TEM. The typical SEM images of d-Ti_3C_2 are shown in Fig. 2a, revealing the d-Ti_3C_2 layer has 2D laminar structure with lateral dimensions in the range of 1–2 μm. The d-Ti_3C_2 nanosheets are almost translucent under TEM (Fig. 2b), attributed to their atomic-scale thickness. This is in line with the atomic force microscopy (AFM) characterization (Fig. S2). The thickness of the d-Ti_3C_2 nanosheets is in the range of 1.7–4.3 nm. After combination, abundant Si nanoparticles are homogenously embedded in the wrinkled d-Ti_3C_2 nanosheets (Figs. 2c and S4). As shown in Fig. 2d, the Si nanoparticles are sandwiched by adjacent crumpled d-Ti_3C_2 layers. They are cross-linked into porous layered structure. The BET analysis of d-Ti_3C_2 and Si/d-Ti_3C_2 hybrids with different mass ratios were also confirm this structure (Fig. S4 and Table S1). The surface

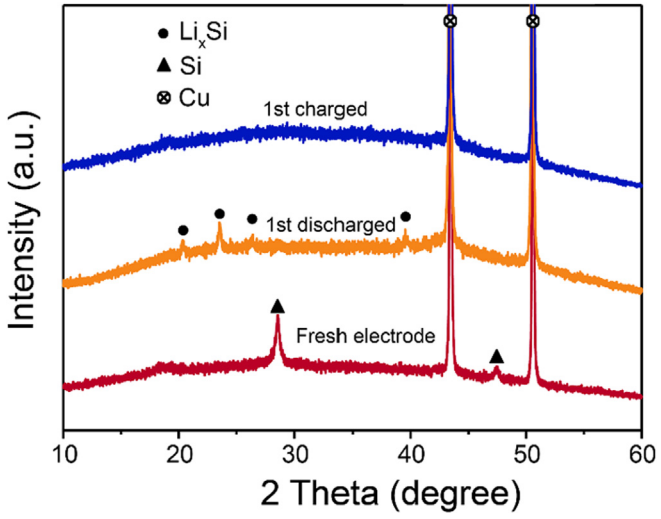

Fig. 5. The XRD patterns of Si/d-Ti_3C_2 hybrids before electrochemical cycling (fresh anode), during the first cycle when material is discharged to 0.01 V and charged to 1.0 V.

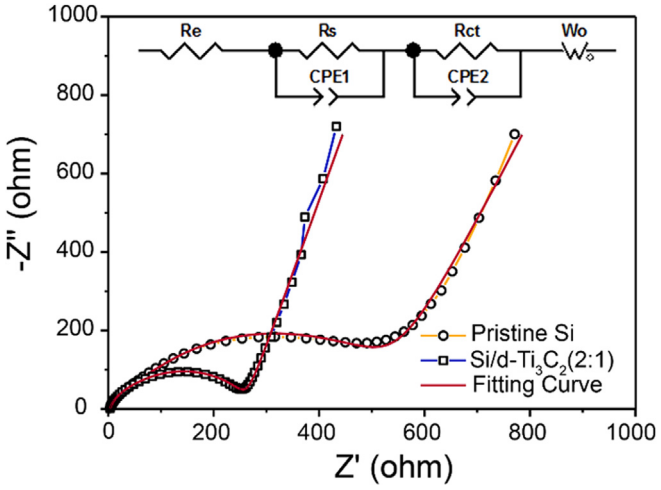

Fig. 6. Nyquist plots of pristine Si and Si/d-Ti_3C_2 hybrids and equivalent circuit of (EIS) measurements.

specific area of d-Ti_3C_2 is 62.63 $m^2 g^{-1}$. It exhibits a typical IV isotherms and H2 hysteresis loop, indicating the stacking pores of aggregated intersheets [46]. After combination, the Si/d-Ti_3C_2 (2:1) hybrids deliver a specific surface area of 28.27 $m^2 g^{-1}$. The disappeared hysteresis demonstrates that the Si NPs are filled into the pores of d-Ti_3C_2 sheets. The (1 1 1) lattice plane of Si can be observed in the Si/d-Ti_3C_2 nanohybrids (Fig. 2e). Thin layers of amorphous SiO_x are formed on the surface of Si nanoparticles, attributed to the partial surface oxidation (Fig. 2f) [47].

The surface functional groups of pristine Si, Si/d-Ti_3C_2 hybrids and d-Ti_3C_2 are firstly elucidated by Fourier-transform infrared spectroscopy (FT-IR). As shown in Fig. 3a, the bands located at 1051, 1620 and 570 cm^{-1} in FT-IR spectrum of d-Ti_3C_2 are signed to the C–O, C═O and Ti–O band vibration, respectively [48]. For the pristine Si and Si/d-Ti_3C_2 hybrids, the asymmetric and symmetric stretching vibrations of the Si–O–Si bonds are observed at 870 and 1120 cm^{-1}, respectively. The band at 1200 cm^{-1} could be attributed to the Si–O bonds [49]. Besides, the shoulder peak observed at 950–1040 cm^{-1} are ascribed to the bending vibration of Si–OH [50]. It should be noted that a weak characteristic vibration of Si–O–Ti bonds appears at 938 cm^{-1} in the hybrids [51], indicating the interaction between the Si nanoparticles and d-Ti_3C_2. It can be observed clearly from the local enlarged FT-IR (Fig. S6). This assumption is also supported by the X-ray photoelectron spectroscopy (XPS) results. The XPS survey spectrum of Si/d-Ti_3C_2 hybrids exhibit the characteristic peaks of Si 2p, O 1s, Ti 2p, C 1s, and F 1s (Fig. 3b). In O 1s XPS spectrum, the binding energy at 529.3, 530.1 and 531.7 eV are ascribed to O–Ti, C–Ti–O_x and O–Si bonds of Si/d-Ti_3C_2 hybrid. The peak at 532.5 eV is related to peroxy –O–O– bonds. The adjoining atoms to each oxygen configuration may be Si or H [52]. It is worth noting that a small peak appears at 531.1 eV in Si/d-Ti_3C_2 hybrids suggesting the formation of Si–O–Ti bonds [53]. The XPS results show great accordance with the FTIR characterization, which inferred that the possible formation mechanism of Si–O–Ti bonds is the partial dehydration of Si–OH and Ti–OH [54]. In the Si 2p XPS spectrum of Si/d-Ti_3C_2 hybrids (Fig. 3d), the binding energies of Si $2p_{1/2}$ and Si $2p_{3/2}$ locate at 98.7 and 99.3 eV, respectively. The Si–O bond shifts to the higher binding energy compared with that of pristine Si, suggesting the different oxidation states of Si. Due to the treatment of Si/d-Ti_3C_2 hybrids, the increase of oxidation degree results in the increased electro-negativity of the Si–O bond [55,56].

The electrochemical performance of Si/d-Ti_3C_2 hybrids as anode materials are evaluated in lithium-ion half-cells. Fig. 4a shows the first three cyclic voltammetry profiles of the Si/d-Ti_3C_2 (2:1) hybrids in the potential window of 0.01–1.0 V. In the first cathode scan, a low reduction peak at 0.35 V appears, indicating the SEI formation (Fig. S7). The reduction peak at 0.2 V in the subsequent cathodic sweep corresponds to the conversion of amorphous Si to Li_xSi, while the two peaks at 0.36 V and 0.51 V in the anodic sweep could be ascribed to the delithiation of Li_xSi back to amorphous Si. The cyclic voltammetry profiles of Si/d-Ti_3C_2 and Si electrodes exhibit similar anodic and cathodic peaks. But the voltage difference (ΔV) between the anodic peaks and cathodic peaks of Si/d-Ti_3C_2 is more smaller than that of pristine Si anode (Fig. S8a). This indicates that the introduction of d-Ti_3C_2 leads to the reduced polarization degree of the Si electrode. Additionally, the intensities of typical peaks increase gradually, suggesting the existence of an activation process. Similar phenomena have been observed before [57].

Fig. 4b displays the early discharge–charge profiles of the Si/d-Ti_3C_2 (2:1) hybrids at a current density of 500 mA g^{-1}. The initial discharge capacity and charge capacity is 2415.4 and 1789.8 mA h g^{-1}, respectively. The initial coulombic efficiency of 74.1%, much smaller than that of carbon-coating Si nanoparticles, could be ascribed to the formation of SEI film. In order to investigate the effect of d-Ti_3C_2, the Si nanoparticles are not modified with carbon wrapping. In the subsequent cycles, the coulombic efficiency increases to above 95%, and then reaches 98% after seven cycles. The shapes of discharge–charge profiles of Si/d-Ti_3C_2 (2:1) hybrids and pristine Si are very similar. The potential plateaus around 0.2 V in the discharge process indicates the conversion of amorphous Si to Li_xSi, while the two plateaus at 0.36 V and 0.51 V in the charge profiles could be ascribed to the delithiation of Li_xSi back to amorphous Si [58]. The shape of the profile and potential plateaus have no obvious change, indicating the stable electrochemical behavior of Si/d-Ti_3C_2 hybrids.

Fig. 4c shows the cycling performance of the Si/d-Ti_3C_2 hybrids with different mass ratios at a current density of 500 mA g^{-1}. The specific capacity is based on the total mass of the Si/d-Ti_3C_2 hybrids. A rapidly capacity fading is observed in the pristine Si nanoparticles from 3519.3 mA h g^{-1} to 563.6 mA h g^{-1} after 100 cycles. In series Si/d-Ti_3C_2 hybrids with different mass ratios, the Si/d-Ti_3C_2 (2:1) hybrids display the highest reversible capacity 1137.6 mA h g^{-1} with a current density of 500 mA g^{-1} after 200 cycles. It is also much higher than that of Si/d-Ti_3C_2 mixture (683.9 mA h g^{-1}) and pure d-Ti_3C_2 (73.9 mA h g^{-1}) (Fig. S9a and b). The surface terminations of d-Ti_3C_2 layers couldn't place a burden on the electrochemical property of electrode [59]. The corresponding areal capacity of Si/d-Ti_3C_2 (2:1) hybrids is 1.04 mAh cm^{-2} at a current density of 0.38 mA cm^{-2} after 100 cycles. Furthermore, we tested the cycling performance of Si/d-Ti_3C_2 (2:1) electrode with the much higher mass loading. When the

mass loading increases to 2.1 mg cm^{-2}, the Si/d-Ti_3C_2 (2:1) electrode displays a capacity of 1192 mAh g^{-1} at 500 mA g^{-1} after 100 cycles. The initial areal capacity of is 2.47 mAh cm^{-2} at 0.22 mA cm^{-2}. From the 6th to 100th cycle at 0.38 mA cm^{-2}, the areal capacity was still reached 1.49 mAh cm^{-2} after 100 cycles (Fig. S9c and d). Hence, Si/d-Ti_3C_2 (2:1) hybrids with high reversible capacity and cycling performance are chosen as the optimal proportion.

Fig. 4d reveals the rate capability of Si/d-Ti_3C_2 (2:1) hybrids at different current densities from 0.2 A g^{-1} to 2 A g^{-1}. The as-synthesized hybrids deliver the discharge capacity of 1948, 1620, 1310, 890 mA h g^{-1} at the current densities of 0.2, 0.5, 1 and 2 A g^{-1}, respectively. It should be note that such values are much higher than those of the pristine Si electrode at the same current density. Besides, the discharge capacity of Si/d-Ti_3C_2 hybrids could recover to the 1600 mA h g^{-1} when the current density returns to 0.2 A g^{-1}.

The microstructure morphology variation of electrodes are shown in Fig. 4e and f. The severe cracks on pristine Si anode's surface after 50 cycles lead to the loss of electrical contact, which is the main reason for drastic capacity degradation of the pristine Si electrode. The insert cross-sectional images in SEM exhibit uneven surface and loose structure. However, the integrity structure of Si/Ti_3C_2 anode has not been destroyed after 50 cycle (Fig. 4f). The high-resolution cross-sectional SEM images of Si/d-Ti_3C_2 hybrids and pristine Si electrodes after 50 cycles have been shown in Fig. S10. The microstructure of Si/d-Ti_3C_2 hybrids still maintains the sandwich structure. The surface of electrode shows no obvious signatures of damage, indicating that the d-Ti_3C_2 nanosheets could alleviate the volume expansion during the lithiation/delithiation process and support integrity of electrodes.

To investigate the structural changes upon lithiation/delithiation, *ex situ* XRD patterns of Si/d-Ti_3C_2 hybrids discharged to 0.01 V and charged to 1.0 V are shown in Fig. 5. The characteristic lattice (1 1 1) of crystalline silicon is observed in the fresh electrode. When the electrode is charged to 0.01 V, the diffraction peaks of crystalline Si almost disappear, and Li_xSi phase emerges at the end of discharge. It suggests the formation of crystalline Li_xSi phase after fully lithiation. However, the XRD scan shows no peaks of silicon after the first charge, indicating that delithiation of crystalline Li_xSi and the formation of amorphous Si [60].

In order to clarify the mechanisms involved, electrochemical impedance spectroscopy (EIS) measurements of the pristine Si and Si/d-Ti_3C_2 hybrid were carried out (Fig. 6). The summarized results of EIS parameters derived using the equivalent circuit model for d-Ti_3C_2/Si hybrids and pristine Si electrodes are list in Table S2. It is found that the diameter of the semicircle of the Si/d-Ti_3C_2 hybrid is obviously smaller than that of pristine Si nanoparticles. It demonstrates that the resistances of the charge transfer reaction of the Si/d-Ti_3C_2 hybrid (Rct = 218.1 Ω) is much smaller than that of pristine Si (Rct = 477.4 Ω). The decreased charge transfer resistance of Si/d-Ti_3C_2 hybrids should be attributed to the excellent conductivity of the d-Ti_3C_2 nanosheets. Besides, the slope of the fitting lines plot defines the Warburg factor, the larger slop of the Si/d-Ti_3C_2 hybrids indicates the reduced resistance in the mass transfer process. The electrical conductivity of pristine Si (2.1×10^{-3} S m^{-1}) and Si/Ti_3C_2 hybrids (1.6 S m^{-1}) are also measured by four-point probe. Therefore, the electrical conductivity of Si based electrode can be significantly improved by adding d-Ti_3C_2 MXene.

4. Conclusions

In conclusion, the porous sandwich-like Si/d-Ti_3C_2 hybrids are fabricated through a facile method. The obtained hybrids exhibit much better electrochemical cycling stability than pristine Si nanoparticles as anode materials for lithium ion batteries. After 200 cycles, a high reversible capacity of more than 1130 mA h g^{-1} can be readily achieved for the Si/d-Ti_3C_2 hybrid. The improved performance can be attributed to two aspects. On the one hand, the d-Ti_3C_2 can effectively alleviate the volume expansion during the lithiation and support integrity of electrodes. On the other hand, it can also increase the electrical contact between the Si nanoparticles and the electrode frame. The Ti_3C_2 layers play an important role in anti-polarization of electrode. This study demonstrates that MXene shows promising prospect in Si-based electrodes.

Acknowledgements

This study is supported by the National Natural Science Funds (No. 21676198) and the Program of Introducing Talents of Discipline to Universities (No. B06006).

Appendix A. Supplementary data

Supplementary data to this article can be found online at https://doi.org/10.1016/j.cej.2019.122212.

References

[1] X. Su, Q.L. Wu, J.C. Li, X.C. Xiao, A. Lott, W.Q. Lu, B.W. Sheldon, J. Wu, Silicon-based nanomaterials for lithium-ion batteries: a review, Adv. Energy Mater. 4 (2014) 1300882.
[2] K. Feng, M. Li, W. Liu, A.G. Kashkooli, X. Xiao, M. Cai, Z. Chen, Silicon-based anodes for lithium-ion batteries: from fundamentals to practical applications, Small 14 (2018) 1702737.
[3] M. Haro, V. Singh, S. Steinhauer, E. Toulkeridou, P. Grammatikopoulos, M. Sowwan, Nanoscale heterogeneity of multilayered Si anodes with embedded nanoparticle scaffolds for Li-ion batteries, Adv. Sci. 4 (2017) 1700180.
[4] F. Song, X. Yang, S. Zhang, L.-L. Zhang, Z. Wen, High-performance phosphorus-modified SiO/C anode material for lithium ion batteries, Ceram. Int. 44 (2018) 18509–18515.
[5] J.Y. Li, Q. Xu, G. Li, Y.X. Yin, L.J. Wan, Y.G. Guo, Research progress regarding Si-based anode materials towards practical application in high energy density Li-ion batteries, Mater. Chem. Front. 1 (2017) 1691–1708.
[6] A. Casimir, H.G. Zhang, O. Ogoke, J.C. Amine, J. Lu, G. Wu, Silicon-based anodes for lithium-ion batteries: effectiveness of materials synthesis and electrode preparation, Nano Energy 27 (2016) 359–376.
[7] Y.T. Bie, J. Yang, X.L. Liu, J.L. Wang, Y.N. Nuli, W. Lu, Polydopamine wrapping silicon cross-linked with polyacrylic acid as high-performance anode for lithium-ion batteries, ACS Appl. Mater. Interfaces 8 (2016) 2899–2904.
[8] Y. Jiang, D. Mu, S. Chen, B. Wu, K. Cheng, L. Li, F. Wu, Electrochemical performance of Si anode modified with carbonized gelatin binder, J. Power Sources 325 (2016) 630–636.
[9] S.H. Ng, J. Wang, D. Wexler, K. Konstantinov, Z.P. Guo, H.K. Liu, Highly reversible lithium storage in spheroidal carbon-coated silicon nanocomposites as anodes for lithium-ion batteries, Angew. Chem. Int. Ed. 45 (2006) 6896–6899.
[10] Y.H. Wang, Y.P. Liu, J.Y. Zheng, H. Zheng, Z.X. Mei, X.L. Du, H. Li, Electrochemical performances and volume variation of nano-textured silicon thin films as anodes for lithium-ion batteries, Nanotechnology 24 (2013) 424011.
[11] H.T. Nguyen, F. Yao, M.R. Zamfir, C. Biswas, K.P. So, Y.H. Lee, S.M. Kim, S.N. Cha, J.M. Kim, D. Pribat, Highly interconnected Si nanowires for improved stability Li-ion battery anodes, Adv. Energy Mater. 1 (2011) 1154–1161.
[12] M.H. Park, M.G. Kim, J. Joo, K. Kim, J. Kim, S. Ahn, Y. Cui, J. Cho, Silicon nanotube battery anodes, Nano Lett. 9 (2009) 3844–3847.
[13] Q. Xu, J.K. Sun, J.Y. Li, Y.X. Yin, Y.G. Guo, Scalable synthesis of spherical Si/C granules with 3D conducting networks as ultrahigh loading anodes in lithium-ion batteries, Energy Storage Mater. 12 (2018) 54–60.
[14] B. Lu, B. Ma, X. Deng, B. Wu, Z. Wu, J. Luo, X. Wang, G. Chen, Dual stabilized architecture of hollow Si@TiO_2@C nanospheres as anode of high-performance li-ion battery, Chem. Eng. J. 351 (2018) 269–279.
[15] H. Zhang, X. Zhang, H. Jin, P. Zong, Y. Bai, K. Lian, H. Xu, F. Ma, A robust hierarchical 3D Si/CNTs composite with void and carbon shell as Li-ion battery anodes, Chem. Eng. J. (2018).
[16] X.H. Liu, L. Zhong, S. Huang, S.X. Mao, T. Zhu, J.Y. Huang, Size-dependent fracture of silicon nanoparticles during lithiation, ACS Nano 6 (2012) 1522–1531.
[17] C.K. Chan, R.N. Patel, M.J. O'Connell, B.A. Korgel, Y. Cui, Solution-grown silicon nanowires for lithium-ion battery anodes, ACS Nano 4 (2010) 1443–1450.
[18] Y. Tian, Y. An, J. Feng, Flexible and free-standing silicon/MXene composite paper for high-performance lithium-ion batteries, ACS Appl. Mater. Interfaces 11 (2019) 10004–10011.
[19] Z. Luo, Q. Xiao, G. Lei, Z. Li, C. Tang, Si nanoparticles/graphene composite membrane for high performance silicon anode in lithium ion batteries, Carbon 98 (2016) 373–380.
[20] Y. Yu, G. Li, S. Zhou, X. Chen, H.-W. Lee, W. Yang, Self-adaptive Si/reduced graphene oxide scrolls for high-performance Li-ion battery anodes, Carbon 120 (2017) 397–404.
[21] Y. Yao, M.T. McDowell, I. Ryu, H. Wu, N. Liu, L. Hu, W.D. Nix, Y. Cui, Interconnected silicon hollow nanospheres for lithium-ion battery anodes with long cycle life, Nano Lett. 11 (2011) 2949–2954.
[22] R. Yi, J.T. Zai, F. Dai, M.L. Gordin, D.H. Wang, Dual conductive network-enabled

graphene/Si–C composite anode with high areal capacity for lithium-ion batteries, Nano Energy 6 (2014) 211–218.
[23] F. Zhang, X. Yang, Y. Xie, N. Yi, Y. Huang, Y. Chen, Pyrolytic carbon-coated Si nanoparticles on elastic graphene framework as anode materials for high-performance lithium-ion batteries, Carbon 82 (2015) 161–167.
[24] Q. Xu, J.Y. Li, J.K. Sun, Y.X. Yin, L.J. Wan, Y.G. Guo, Watermelon-inspired Si/C microspheres with hierarchical buffer structures for densely compacted lithium-ion battery anodes, Adv. Energy Mater. 7 (2017) 1601481.
[25] G. Xia, N. Li, D. Li, R. Liu, C. Wang, Q. Li, X. Lü, J.S. Spendelow, J. Zhang, G. Wu, Graphene/Fe_2O_3/SnO_2 ternary nanocomposites as a high-performance anode for lithium ion batteries, ACS Appl. Mater. Interfaces 5 (2013) 8607–8614.
[26] N. Liu, H. Wu, M.T. McDowell, Y. Yao, C.G. Wang, Y. Cui, A yolk-shell design for stabilized and scalable Li-ion battery alloy anodes, Nano Lett. 12 (2012) 3315–3321.
[27] Y.Z. Li, K. Yan, H.W. Lee, Z.D. Lu, N. Liu, Y. Cui, Growth of conformal graphene cages on micrometre-sized silicon particles as stable battery anodes, Nat. Energy 1 (2016) 15029.
[28] X. Guo, J.Q. Zhang, J.J. Song, W.J. Wu, H. Liu, G.X. Wang, MXene encapsulated titanium oxide nanospheres for ultra-stable and fast sodium storage, Energy Storage Mater. 14 (2018) 306–313.
[29] Y. Zhong, X.H. Xia, F. Shi, J.Y. Zhan, J.P. Tu, H.J. Fan, Transition metal carbides and nitrides in energy storage and conversion, Adv. Sci. 3 (2016) 1500286.
[30] C. Chen, X. Xie, B. Anasori, A. Sarycheva, T. Makaryan, M. Zhao, P. Urbankowski, L. Miao, J. Jiang, Y. Gogotsi, MoS_2-on-MXene heterostructures as highly reversible anode materials for lithium-ion batteries, Angew. Chem. Int. Ed. 57 (2018) 1846–1850.
[31] P. Yu, G.J. Cao, S. Yi, X. Zhang, C. Li, X.Z. Sun, K. Wang, Y.W. Ma, Binder-free 2D titanium carbide (MXene)/carbon nanotube composites for high-performance lithium-ion capacitors, Nanoscale 10 (2018) 5906–5913.
[32] Y. Dall'Agnese, P. Rozier, P.-L. Taberna, Y. Gogotsi, P. Simon, Capacitance of two-dimensional titanium carbide (MXene) and MXene/carbon nanotube composites in organic electrolytes, J. Power Sources 306 (2016) 510–515.
[33] M.-Q. Zhao, X. Xie, C.E. Ren, T. Makaryan, B. Anasori, G. Wang, Y. Gogotsi, Hollow MXene spheres and 3D macroporous MXene frameworks for Na-ion storage, Adv. Mater. 29 (2017) 1702410.
[34] J.N. Xuan, Z.Q. Wang, Y.Y. Chen, D.J. Liang, L. Cheng, X.J. Yang, Z. Liu, R.Z. Ma, T. Sasaki, F. Geng, Organic-base-driven intercalation and delamination for the production of functionalized titanium carbide nanosheets with superior photothermal therapeutic performance, Angew. Chem. 128 (2016) 14789–14794.
[35] W. Bao, L. Liu, C. Wang, S. Choi, D. Wang, G. Wang, Facile synthesis of crumpled nitrogen-doped MXene nanosheets as a new sulfur host for lithium-sulfur batteries, Adv. Energy Mater. 13 (2018) 1702485.
[36] C.J. Zhang, S.-H. Park, A. Seral-Ascaso, S. Barwich, N. McEvoy, C.S. Boland, J.N. Coleman, Y. Gogotsi, V. Nicolosi, High capacity silicon anodes enabled by MXene viscous aqueous ink, Nat. Commun. 10 (2019) 849.
[37] X. Wu, Z. Wang, M. Yu, L. Xiu, J. Qiu, Stabilizing the MXenes by carbon nanoplating for developing hierarchical nanohybrids with efficient lithium storage and hydrogen evolution capability, Adv. Mater. 29 (2017) 1607017.
[38] L.Y. Yu, L.F. Hu, B. Anasori, Y.T. Liu, Q.Z. Zhu, P. Zhang, Y. Gogotsi, B. Xu, MXene-bonded activated carbon as a flexible electrode for high-performance supercapacitors, ACS Energy Lett. 3 (2018) 1597–1603.
[39] H. Tang, W.L. Li, L.M. Pan, C.P. Cullen, Y. Liu, A. Pakdel, D.H. Long, J. Yang, N. McEvoy, G.S. Duesberg, V. Nicolosi, C.F. Zhang, In situ formed protective barrier enabled by sulfur@titanium carbide (MXene) ink for achieving high-capacity, long lifetime Li-S batteries, Adv. Sci. 5 (2018) 1800502.
[40] Y. Wu, P. Nie, L. Wu, H. Dou, X. Zhang, 2D MXene/SnS_2 composites as high-performance anodes for sodium ion batteries, Chem. Eng. J. 334 (2018) 932–938.
[41] X. Xie, S. Wang, K. Kretschmer, G. Wang, Two-dimensional layered compound based anode materials for lithium-ion batteries and sodium-ion batteries, J. Colloid Interface Sci. 499 (2017) 17–32.
[42] X. Zhou, Y.-X. Yin, L.-J. Wan, Y.-G. Guo, Facile synthesis of silicon nanoparticles inserted into graphene sheets as improved anode materials for lithium-ion batteries, Chem. Commun. 48 (2012) 2198–2200.
[43] J. Yan, C.E. Ren, K. Maleski, C.B. Hatter, B. Anasori, P. Urbankowski, A. Sarycheva, Y. Gogotsi, Flexible MXene/graphene films for ultrafast supercapacitors with outstanding volumetric capacitance, Adv. Funct. Mater. 27 (2017) 1701264.
[44] X. Xie, K. Kretschmer, B. Anasori, B. Sun, G. Wang, Y. Gogotsi, Porous $Ti_3C_2T_x$ MXene for ultrahigh-rate sodium-ion storage with long cycle life, ACS Appl. Nano Mater. 1 (2018) 505–511.
[45] I.D. Wolf, Stress measurements in Si microelectronics devices using Raman spectroscopy, J. Raman Spectrosc. 30 (1999) 877–883.
[46] L. Xiu, Z. Wang, M. Yu, X. Wu, J. Qiu, Aggregation-resistant 3D MXene-based architecture as efficient bifunctional electrocatalyst for overall water splitting, ACS Nano 12 (2018) 8017–8028.
[47] H. Tao, L. Xiong, S. Zhu, X. Yang, L. Zhang, Flexible binder-free reduced graphene oxide wrapped Si/carbon fibers paper anode for high-performance lithium ion batteries, Int. J. Hydrogen Energy 41 (2016) 21268–21277.
[48] R.Z. Zhao, M.Q. Wang, D.Y. Zhao, H. Li, C.X. Wang, L.W. Yin, Molecular-level heterostructures assembled from titanium carbide MXene and Ni–Co–Al layered double-hydroxide nanosheets for all-solid-state flexible asymmetric high-energy supercapacitors, ACS Energy Lett. 3 (2017) 132–140.
[49] J. Wu, W.M. Tu, Y. Zhang, B.L. Guo, S.S. Li, Y. Zhang, Y.D. Wang, M. Pan, Polydopamine coated graphite oxide/silicon composite as anode of lithium ion batteries, Powder Technol. 311 (2017) 200–205.
[50] M. Zhou, F. Pu, Z. Wang, T.W. Cai, H. Chen, H.Y. Zhang, S.Y. Guan, Facile synthesis of novel Si nanoparticles-graphene composites as high-performance anode materials for Li-ion batteries, Phys. Chem. Chem. Phys. 15 (2013) 11394–11401.
[51] S. Rasalingam, R. Peng, R.T. Koodali, Removal of hazardous pollutants from wastewaters: applications of TiO_2-SiO_2 mixed oxide materials, J. Nanomater. 2014 (2014) 1–42.
[52] A. Mehonic, M. Buckwell, L. Montesi, L. Garnett, S. Hudziak, S. Fearn, R. Chater, D. McPhail, A.J. Kenyon, Structural changes and conductance thresholds in metal-free intrinsic SiO_x resistive random access memory, J. Appl. Phys. 117 (2015) 124505.
[53] X.T. Gao, I.E. Wachs, Titania–silica as catalysts: molecular structural characteristics and physico-chemical properties, Catal. Today 51 (1999) 233–254.
[54] S. Cheng, X. Liu, S. Yun, H. Luo, Y. Gao, SiO_2/TiO_2 composite aerogels: preparation via ambient pressure drying and photocatalytic performance, Ceram. Int. 40 (2014) 13781–13786.
[55] J.A.L. López, J.C. López, D.V. Valerdi, G.G. Salgado, T. Díaz-Becerril, A.P. Pedraza, F.F. Gracia, Morphological, compositional, structural, and optical properties of Si-NC embedded in SiO_x films, Nanoscale Res. Lett. 7 (2012) 604.
[56] J. Wang, M. Zhou, G. Tan, S. Chen, F. Wu, J. Lu, K. Amine, Encapsulating micro-nano Si/SiO_x into conjugated nitrogen-doped carbon as binder-free monolithic anodes for advanced lithium ion batteries, Nanoscale 7 (2015) 8023–8034.
[57] H. Mi, F. Li, S. Xu, Z. Li, X. Chai, C. He, Y. Li, J. Liu, A tremella-like nanostructure of silicon@void@graphene-like nanosheets composite as an anode for lithium-ion batteries, Nanoscale Res. Lett. 11 (2016) 204.
[58] H. Tao, S. Zhu, L. Xiong, L. Zhang, X. Yang, Reduced graphene oxide wrapped Si/C assembled on 3D N-doped carbon foam as binder-free anode for enhanced lithium storage, ChemistrySelect 2 (2017) 2832–2840.
[59] Y. Xie, M. Naguib, V.N. Mochalin, M.W. Barsoum, Y. Gogotsi, X. Yu, K.-W. Nam, X.-Q. Yang, A.I. Kolesnikov, P.R. Kent, Role of surface structure on Li-ion energy storage capacity of two-dimensional transition-metal carbides, J. Am. Chem. Soc. 136 (2014) 6385–6394.
[60] B. Laïk, D. Ung, A. Caillard, C. Sorin Cojocaru, D. Pribat, J.-P. Pereira-Ramos, An electrochemical and structural investigation of silicon nanowires as negative electrode for Li-ion batteries, J. Solid State Electrochem. 14 (2010) 1835–1839.